

This is a copy of the published version, or version of record, available on the publisher's website. This version does not track changes, errata, or withdrawals on the publisher's site.

## Effects of Ga doping on the phase transitions of V2O3

Pavitra N. Shanbhag, Anjana Joseph, Fabio Orlandi, Pascal Manuel, R. Mahendiran, Francois Fauth, Chandrabhas Narayana, A. Sundaresan, and C. N. R. Rao

### Published version information


**Citation:** PN Shanbhag et al. Effects of Ga doping on the phase transitions of V2O3. Phys Rev B 105, no. 6 (2022): 064103

**DOI:** [10.1103/PhysRevB.105.064103](https://doi.org/10.1103/PhysRevB.105.064103)

This version is made available in accordance with publisher policies. Please cite only the published version using the reference above. This is the citation assigned by the publisher at the time of issuing the APV. Please check the publisher's website for any updates.

This item was retrieved from **ePubs**, the Open Access archive of the Science and Technology Facilities Council, UK. Please contact [epublications@stfc.ac.uk](mailto:epublications@stfc.ac.uk) or go to <http://epubs.stfc.ac.uk/> for further information and policies.

## Effects of Ga doping on the phase transitions of $V_2O_3$

Pavitra N. Shanbhag <sup>1</sup>, Anjana Joseph <sup>1</sup>, Fabio Orlandi <sup>2</sup>, Pascal Manuel <sup>2</sup>, R. Mahendiran <sup>3</sup>, Francois Fauth <sup>4</sup>,  
Chandrabhas Narayana <sup>1</sup>, A. Sundaresan <sup>1</sup> and C. N. R. Rao <sup>1</sup>

<sup>1</sup>*School of Advanced Materials, and Chemistry and Physics of Materials Unit, Jawaharlal Nehru Centre for Advanced Scientific Research, Jakkur P.O., Bangalore 560064, India*

<sup>2</sup>*ISIS Facility, Rutherford Appleton Laboratory, Chilton, Didcot OX11 0QX, United Kingdom*

<sup>3</sup>*Physics Department, 2 Science Drive 3, Faculty of Science, National University of Singapore, Singapore 117551, Singapore*

<sup>4</sup>*CELLS-ALBA Synchrotron, E-08290 Cerdanyola del Vallès, Barcelona, Spain*



(Received 5 July 2021; revised 11 December 2021; accepted 18 January 2022; published 14 February 2022)

$V_2O_3$  undergoes a first-order metal-insulator transition accompanied by a magnetostructural transition at  $T_{MI} \sim 160$  K. Here, we report a comprehensive study on gallium-doped (4%) polycrystalline  $V_2O_3$  by employing various experimental techniques such as synchrotron x-ray diffraction, thermal expansion, Raman spectroscopy, DC magnetization, time-of-flight neutron diffraction, heat capacity, and electrical transport. Our studies show several interesting features related to the structural, magnetic, and electronic phase transitions in Ga-doped sample. Intriguingly, the nonmagnetic doping in  $V_2O_3$  enhances the Néel temperature by 25 K ( $T_N = 185$  K). Further, we find the decoupling of the structural transition from the magnetic and insulator-insulator transition ( $T_{II} \sim 185$  K). Raman spectroscopic studies reveal that the structural phase transition begins at  $T^*$  ( $= 195$  K), which is slightly above  $T_N$  or  $T_{II}$ , as evidenced from the softening of  $E_g$  mode and the splitting of  $A_{1g}$  mode. Additionally, the rhombohedral and monoclinic phases coexist in a broad temperature range, and a complete phase transformation to monoclinic phase occurs at 127 K.

DOI: [10.1103/PhysRevB.105.064103](https://doi.org/10.1103/PhysRevB.105.064103)

### I. INTRODUCTION

The origin of the first-order metal-insulator transition (MIT) in the sesquioxide  $V_2O_3$  has remained the subject of an extensive investigation because of the intricacy of the MIT involving structural and magnetic transitions. At high temperatures,  $V_2O_3$  is metallic and has a rhombohedral structure ( $R\bar{3}c$ ). Below  $T \sim 160$  K, it undergoes a first-order MIT with a change in resistance of several orders in magnitude and a phase transition to monoclinic structure ( $I2/a$ ) [1,2]. Further, it undergoes a paramagnetic-to-antiferromagnetic (AFM) transition at the same temperature. The origin of the MIT in  $V_2O_3$  has been explained using various theoretical models, yet there is no consensus on understanding the mechanism. The most satisfactory model invokes a Mott-Hubbard scenario where electron-electron correlations play an important role [3–5]. According to this theory, the onsite Coulomb repulsion  $U$  drives the splitting of the conduction band into two bands, i.e., an upper Hubbard band and a lower Hubbard band separated by an energy gap. The ratio between the energy gap and onsite Coulomb repulsion decides whether the system is a metal or an insulator. For negligible electron-electron correlation, the system acts as a metal, whereas for the highly correlated system, the electrons are localized and become an insulator [3–5]. Slater [6] claimed that the AFM ordering drives the gap opening where electronic energies become spin-dependent [7]. Since all three transitions occur at the same temperature, it remains a challenge to identify the actual mechanism responsible for the MIT.

To decipher the low-temperature MIT mechanism, many studies have been carried out on  $V_2O_3$ , including doping of various transition metal ions and applying external pressures that significantly influence structural, magnetic, and electronic properties. Doping Ti in  $V_2O_3$  reduces  $T_N$  and the accompanying MIT. The AFM insulating state is completely suppressed for 5% Ti doping, and the metallic state with rhombohedral structure remains at the lowest temperature [1,8,9]. Cr-doped  $V_2O_3$  is the first prototypical example reported for the physics of the Mott-Hubbard transition [10,11]. Doping with 0.5 to 1.7% of Cr in  $V_2O_3$  exhibits two different metal-insulator phase transitions. The first transition occurs at 180 K corresponding to the low-temperature AFM insulator (AFI) to high-temperature paramagnetic metal (PMM) accompanying a magnetostructural transition. The second transition, from the PMM to the high-temperature paramagnetic insulating (PMI) phase, occurs between 250 and 350 K. The high-temperature transition is accompanied by a decrease in the  $c/a$  ratio of the corundum unit cell from 2.83 (PMM) to 2.79 (PMI) without change in the crystal symmetry [12,13]. Similar behavior is observed in Al-doped (1 at.%)  $V_2O_3$  [14]. Apart from this, nonmagnetic trivalent  $Mo^{3+}$  doping in  $V_2O_3$  results in a decrease of  $T_N$  and is suppressed beyond the 10% doping level [15]. A wide range of divalent cation substitution, for example,  $V_{2-x}Ni_xO_3$  ( $0 < x < 0.75$ ), results in the semiconducting behavior without any indication of MIT [16]. The rhombohedral ( $R\bar{3}c$ )-to-monoclinic ( $P2_1/c$ ) structural phase transition in  $V_2O_3$  is also observed under high pressure (32.5 GPa) at 300 K [17].

Toward understanding the longstanding problem of identifying relevant mechanisms responsible for the MIT in  $V_2O_3$ , we have investigated the effects of doping of nonmagnetic ions (4% of  $Ga^{3+}$ ) on the MIT, magnetism, crystal structure, and thermal properties. The Ga doping transforms the metallic conductivity in the paramagnetic state to a weakly insulating behavior, and an insulator-insulator transition occurs without hysteresis at  $T_{II} \sim 185$  K, which is 25 K higher than that observed in undoped  $V_2O_3$ . Additionally, Ga-doped  $V_2O_3$  shows a paramagnetic-to-AFM transition at  $T_N \sim 185$  K, which is well above the magnetic transition observed in undoped  $V_2O_3$ . Further, Raman spectroscopic studies reveal that the structural transition starts at  $T^* \sim 195$  K, confirming the decoupling of structural transition from magnetic and electronic transitions in Ga-doped  $V_2O_3$ .

## II. EXPERIMENTAL

A polycrystalline sample of Ga-doped  $V_2O_3$  was prepared by the solid-state reaction method. The starting materials  $V_2O_5$  and  $Ga_2O_3$  were mixed in a 1:1 ratio and heated in a hydrogen atmosphere at 1000 °C with several intermediate grindings. We should mention here that we failed in preparing a Ga-doped  $V_2O_3$  sample starting from a stoichiometric amount of  $Ga_2O_3$  and  $V_2O_3$  even under high-pressure and high-temperature conditions. However, the reaction of a 1:1 mixture of  $Ga_2O_3$  and  $V_2O_5$  in the hydrogen atmosphere resulted in 4% doping of Ga in  $V_2O_3$ . Under the hydrogen atmosphere,  $Ga_2O_3$  reduces to metallic Ga. Due to its low melting point, most of the metallic Ga likely evaporates during the synthesis. During this process, a small amount of Ga (4%) is substituted at the V site. The variable temperature synchrotron x-ray diffraction (XRD) data were collected with the wavelength 0.49583 Å using the position-sensitive detector MYTHEN at the Material Science Powder Diffraction beamline BL04\_MSPPS of the ALBA synchrotron facility (Barcelona area, Spain) [18,19]. Thermal expansion measurements were done using a miniature capacitance dilatometer probe attached to the physical property measurement system (PPMS). The Raman spectroscopic measurements were carried out in  $V_2O_3$  and Ga-doped  $V_2O_3$  samples using a confocal micro-Raman spectrometer (LABRAM HR Evolution) with the 532 nm excitation frequency-doubled Nd:YAG laser in the backscattering mode with an 1800 grooves/mm grating. The temperature-dependent Raman studies were carried out using a temperature stage (LINKAM THMS 600) with the help of a long working distance 50× objective. A laser power of 0.1 mW was used for all the measurements with 400 s accumulation time per scan. We have deliberately avoided high laser powers to avoid laser heating of the sample. Polycrystalline pellets were used for all the measurements, and the cooling rate was kept low at 2 K/min. Before each measurement, the sample temperature was stabilized with accuracy better than 1 K. Magnetic measurements were performed using a superconducting quantum interference device magnetometer in the vibrating sample mode. Time-of-flight neutron powder diffraction (NPD) data were collected on the WISH instrument in the ISIS neutron and muon facility, United Kingdom. Crystal and magnetic structure analysis was carried out by the Rietveld refinement method using JANA2006

[20–22]. Inductively coupled plasma optical emission spectroscopy (ICP-OES) studies were carried out using a Perkin Elmer Avio 200 instrument to determine the composition of the sample. Heat capacity was measured in the PPMS. Differential scanning calorimetry (DSC) data were collected using the TA Q2000 instrument in modulated mode. The data were recorded in the temperature range of 150–250 K with a 3 °C/min ramp rate under a nitrogen atmosphere. Resistivity measurement was registered in a four-probe method using the ETO option in the PPMS, EC II.

## III. RESULTS AND DISCUSSION

To explore the structural phase transition in Ga-doped  $V_2O_3$ , temperature-dependent synchrotron XRD data were collected from 300 to 120 K at several temperatures. The data collected at 300 K confirmed that the compound crystallizes in rhombohedral structure with the space group  $R\bar{3}c$ . However, some of the reflections [(1 0 4), (0 0 6), (1 -1 8), (1 0 10), ...] and [(2 -1 0), (3 0 0), (4 -2 0), ...] exhibit asymmetry with an extending Lorentzian tail on higher and lower angles, respectively. Also, there was no trend in Bragg planes observed on account of peak asymmetry. Such an unusual anisotropic peak broadening or asymmetry was also observed in the  $RVO_3$  [23]. This anisotropic peak broadening could arise from possible oxygen inhomogeneities created during the synthesis of the sample under a reducing atmosphere. Generally, the presence of such oxygen inhomogeneities in the sample causes variation of cell parameters giving rise to nonuniform unit cells in the crystallites [24,25]. Rietveld refinement performed on XRD data at 300 K using JANA2006 [22] considering the  $R\bar{3}c$  model with one set of lattice parameters could not fit these asymmetric peaks well, as shown in Fig. S1 in the Supplemental Material [26]. Hence, we performed refinements using two similar sets of slightly variable lattice parameters in the  $R\bar{3}c$  space group, which resulted in better refinement and reliability factors. The concentration of Ga in two different phases is found to be  $\sim 4\%$ . The Rietveld refined synchrotron XRD profile collected at 300 K and the crystal structure are shown in Figs. 1(a) and 1(b), respectively. The crystal structure consists of trigonally distorted octahedra of oxygen ligands with the central vanadium atom forming a pair with the neighboring vanadium atom along the  $c$  axis. Upon cooling, the evolution of the new peaks due to monoclinic distortion in the rhombohedral unit cell across the structural phase transition and coexistence of the rhombohedral and the monoclinic phases can be viewed in Fig. S2 in the Supplemental Material [26]. Further, a complete transformation of the rhombohedral to the monoclinic phase was observed at 127 K. Since we observe anisotropic peak broadening and asymmetry in Ga-doped  $V_2O_3$  at ambient conditions, we expect such a lattice parameter distribution would also be present at low temperatures. Therefore, we carried out Rietveld refinement for synchrotron XRD data at low temperatures with an additional set of slightly different lattice parameters using the  $I2/c$  model. The refined synchrotron XRD profile collected at 120 K and crystal structure are shown in Figs. 1(c) and 1(d), respectively. The refined structural parameters obtained from 300 and 120 K data are displayed in Tables I and II, respectively. In Figs. 2(a)–2(f), we show the

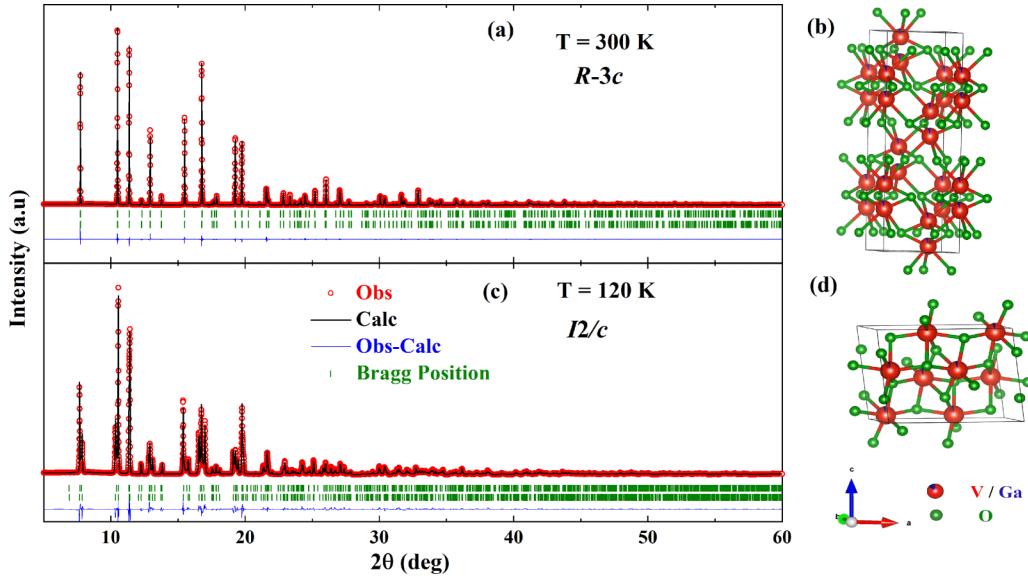


FIG. 1. Rietveld refined synchrotron x-ray ( $\lambda = 0.49583 \text{ \AA}$ ) diffraction profiles of Ga-doped  $\text{V}_2\text{O}_3$  at (a) 300 K and (c) 120 K. The two Bragg positions are associated with the two different sets of lattice parameters under the space group  $R\bar{3}c$  in (a) and  $I2/c$  in (c). Crystal structure of Ga-doped  $\text{V}_2\text{O}_3$  at (b) 300 K and (d) 120 K.

variation of lattice parameters,  $c/a$  ratio, V-V bond distance between face shared octahedra, and unit cell volume as a function of temperature. It is to be noted that the lattice parameters [shown in Figs. 2(a)–2(e)] from 300 to 180 K correspond to the major phase (55.37%) with low statistical errors. At 195 K, there is a slight variation of lattice parameters in the rhombohedral phase [shown as a red-colored vertical dashed line in Figs. 2(a)–2(d)], indicating local changes in the lattice due to the onset of the structural phase transition, which is discussed in detail in the Raman spectroscopic studies later. We can see a drastic change in values of all three lattice parameters at 180 K. Interestingly, lattice parameter  $a$  of the rhombohedral phase shows an increase at 180 K and decreases with further cooling. Observing the unit cell parameters across the structural phase transition at 180 K, it is clear that the rhombohedral unit cell expanded along  $a$  and  $b$  axes and

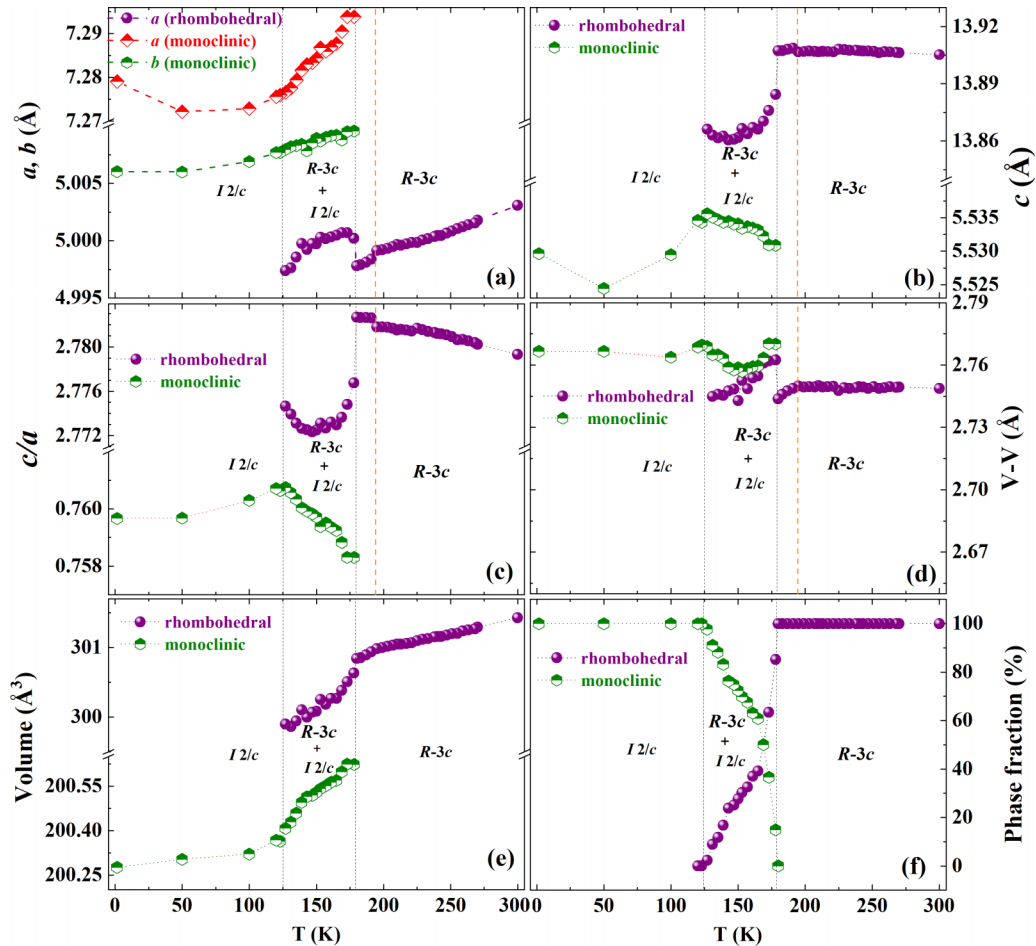
contracted along the  $c$  axis in the monoclinic phase, as shown in Figs. 2(a) and 2(b), respectively. Since  $\text{Ga}^{3+}$  ( $0.62 \text{ \AA}$ ) is smaller than  $\text{V}^{3+}$  ( $0.64 \text{ \AA}$ ), the  $c$  parameter decreased from  $14.003(1)$  to  $13.9052(9) \text{ \AA}$ , whereas interestingly, the  $a$  value increased from  $4.9515(3)$  to  $5.00309(2) \text{ \AA}$ . Thus, the unit cell volume increased from  $298.03$  to  $301.42 \text{ \AA}^3$  after 4% Ga doping in  $\text{V}_2\text{O}_3$  [11]. Also, Chen *et al.* [27] reported that 3% doping of comparatively similar-sized  $\text{Cr}^{3+}$  ( $0.615 \text{ \AA}$ ) in  $\text{V}_2\text{O}_3$  showed an increase of  $a$  and decrease of  $c$  parameters to  $4.998$  and  $13.924 \text{ \AA}$ , respectively. Hence, the volume increased to  $301.33 \text{ \AA}^3$ . Changes in lattice parameters can be viewed in the temperature-dependent  $c/a$  plot where  $c/a$  values for the rhombohedral phase and the newly evolving monoclinic phase drop significantly across  $T \sim 180 \text{ K}$  [Fig. 2(c)]. As a result of Ga doping, the  $c/a$  value at room temperature decreased from  $2.828$  to  $2.7793(9)$ . This is like 3.8% Cr-doped  $\text{V}_2\text{O}_3$ , where

TABLE I. Rietveld refined structural parameters of Ga-doped  $\text{V}_2\text{O}_3$  obtained from synchrotron x-ray powder diffraction data collected at 300 K.

Space group: $R\bar{3}c$ (rhombohedral)					
Atomic coordinates	Occupancy	$x$	$y$	$z$	Uiso ( $\text{\AA}^2$ )
Phase I (55.37%): $a = b = 5.00309(2) \text{ \AA}$ , $c = 13.9052(9) \text{ \AA}$ , and $\alpha = \beta = 90^\circ$ , $\gamma = 120^\circ$ ; $R_p = 1.29$ and $R_{wp} = 2.09\%$					
V (12c)	0.961(2)	0.3333	0.6667	0.01550(5)	0.00148(7)
Ga (12c)	0.039(2)	0.3333	0.6667	0.01550(5)	0.00148(7)
O (18e)	1.0	-0.0267(3)	0.6400(3)	0.08333	0.0006(2)
Phase II (44.63%): $a = b = 5.00930(4) \text{ \AA}$ , $c = 13.8624(30) \text{ \AA}$ , and $\alpha = \beta = 90^\circ$ , $\gamma = 120^\circ$ ; $R_p = 1.16$ and $R_{wp} = 1.86\%$					
V (12c)	0.958(1)	0.3333	0.6667	0.01690(4)	0.00271(11)
Ga (12c)	0.042(1)	0.3333	0.6667	0.01690(4)	0.00271(11)
O (18e)	1.0	-0.0265(4)	0.6402(4)	0.08333	0.0034(4)
Overall goodness of fit parameters: GOF = 5.41, $R_p = 3.11$ , and $R_{wp} = 4.71\%$					

TABLE II. Rietveld refined structural parameters of Ga-doped  $V_2O_5$  obtained from synchrotron x-ray powder diffraction data collected at 120 K.

Space group: $I2/c$ (monoclinic)					
Atomic coordinates	Occupancy	$x$	$y$	$z$	Uiso ( $\text{\AA}^2$ )
Phase I (57.87%): $a = 7.27555(9) \text{\AA}$ , $b = 5.00956(7) \text{\AA}$ , $c = 5.53458(9) \text{\AA}$ , and $\alpha = \gamma = 90^\circ$ , $\beta = 96.637(12)^\circ$ ; $R_p = 6.88$ and $R_{wp} = 9.62\%$					
V (8 <i>f</i> )	0.961	0.5961(1)	0.2522(2)	0.5983(2)	0.00347(2)
Ga (8 <i>f</i> )	0.039	0.5961(1)	0.2522(2)	0.5983(2)	0.00347(2)
O (8 <i>f</i> )	1.0	0.6605(5)	1.0998(8)	0.8936(6)	0.00284(4)
O (4 <i>e</i> )	1.0	0.5	0.4195(10)	0.25	0.00284(4)
Phase II (42.13%): $a = 7.31963(46) \text{\AA}$ , $b = 5.01122(18) \text{\AA}$ , $c = 5.49605(42) \text{\AA}$ , and $\alpha = \gamma = 90^\circ$ , $\beta = 96.521(39)^\circ$ ; $R_p = 3.83$ and $R_{wp} = 6.04\%$					
V (8 <i>f</i> )	0.958	0.5954(2)	0.2535(3)	0.5471(3)	0.00347(2)
Ga (8 <i>f</i> )	0.042	0.5954(2)	0.2535(3)	0.5471(3)	0.00347(2)
O (8 <i>f</i> )	1.0	0.6424(8)	1.0823(15)	0.9072(14)	0.00284(4)
O (4 <i>e</i> )	1.0	0.5	0.458(2)	0.25	0.00284(4)
Goodness of fit parameters: GOF = 11.57, $R_p = 7.76$ , and $R_{wp} = 10.10\%$					

FIG. 2. Variation of (a) and (b) lattice constant, (c)  $c/a$  value, (d) V-V distance between face-shared octahedra, (e) volume of unit cell, and (f) phase fractions with respect to temperature for rhombohedral and monoclinic structures.

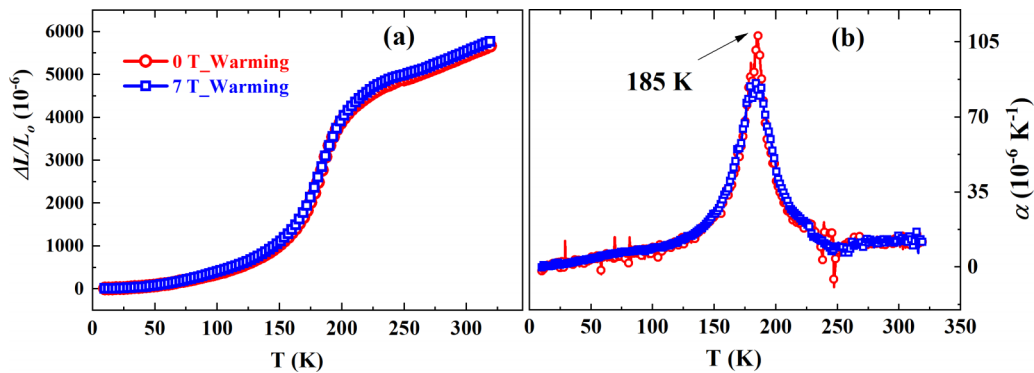


FIG. 3. (a) Normalized linear thermal expansion ( $\frac{\Delta L}{L_0}$ ) as a function of temperature measured with capacitance dilatometer and (b) calculated coefficient of thermal expansion  $\alpha = \frac{1}{T} \partial(\frac{\Delta L}{L_0})$  with respect to temperature of Ga-doped  $V_2O_3$ .

the  $c/a$  value is 2.783 [28]. Further, the V-V distance for face-shared octahedra in the rhombohedral phase increased from 2.697(1) to 2.74868(6) Å upon Ga doping in  $V_2O_3$ . In the case of 3.8%  $Cr^{3+}$  doping in  $V_2O_3$ , the V-V distance increased to 2.746(1) Å [28]. The V-V distance for face-shared octahedra across 180 K increased as the symmetry changed from rhombohedral to monoclinic, as shown in Fig. 2(d). From the temperature-dependent volume data [Fig. 2(e)], the unit cell significantly contracted by  $1.53 \text{ \AA}^3$  ( $\Delta V$ ) compared with room temperature, indicating a first-order structural phase transition at 180 K. The evolution of temperature-dependent phase fractions across the structural phase transition is shown in Fig. 2(f), which reveals the phase coexistence in the temperature range 127–180 K. Below 127 K, only the monoclinic phase ( $I2/c$ ) exists. The structural parameters, as shown in Figs. 2(a)–2(e) < 120 K, are obtained by NPD analysis which is discussed later.

Further, temperature-dependent linear thermal expansion studies of Ga-doped  $V_2O_3$  were carried out across the structural phase transition. The fractional change in thermal expansion ( $\frac{\Delta L}{L_0}$ ), where  $L_0$  is the value measured at 300 K, shows a rapid contraction between 220 and 150 K, as shown in Fig. 3(a). The linear thermal expansion coefficient  $\alpha = \frac{1}{T} \partial(\frac{\Delta L}{L_0})$  shows a clear anomaly at 185 K [Fig. 3(b)], corresponding to large volume contraction across the rhombohedral-to-monoclinic structural transition, as revealed by the synchrotron XRD study [Fig. 2(e)]. It is noteworthy that an applied magnetic field of 7 T does not affect the thermal expansion significantly around the phase transition temperature. The small difference seen at higher temperatures could be due to thermal hysteresis.

To study the structural phase transition and its microscopic origin, we carried out Raman spectroscopic measurements in undoped  $V_2O_3$  and Ga-doped  $V_2O_3$ . Raman spectra of Ga-doped  $V_2O_3$  recorded at 300 and 100 K with mode assignments corresponding to various vibrational symmetries are shown in Fig. 4 [29]. At room temperature, the crystal structure of  $V_2O_3$  is  $\alpha$ -corundum with the  $R\bar{3}c$  space group and the  $D_{3d}$  point group [29]. Seven Raman active modes are expected for a crystal of  $D_{3d}$  point group: two  $A_{1g}$  modes and five  $E_g$  modes [29,30]. Each  $A_{1g}$  mode can be considered as a superposition of two simple vibrations of the same symmetry [31]. In the first vibration, vanadium atoms move toward the

oxygen plane and back along the  $z$  axis. In the second one, oxygen atoms together move toward the  $z$  axis and back in the basal plane. These vibrations result in the lower wave number and higher wave number  $A_{1g}$  modes, respectively. The first and second  $E_g$  modes result from the out-of-phase and in-phase movement of vanadium atoms, respectively [32]. The room temperature spectra of  $V_2O_3$  (Fig. S3 in the Supplemental Material [26]) consist of two asymmetric shaped  $A_{1g}$  modes at 235 and 501  $\text{cm}^{-1}$  and three  $E_g$  modes at 210, 293, and 586  $\text{cm}^{-1}$ . The asymmetric line shape of the  $A_{1g}$  mode could be resulting from the Fano resonance effect [33].

From Fig. 4, we see two broad asymmetric shaped  $A_{1g}$  modes at 247 and 512  $\text{cm}^{-1}$  and three  $E_g$  modes at 229, 308, and 589  $\text{cm}^{-1}$ . Raman modes of the doped compound are shifted to higher frequencies than the undoped compound with  $\Delta\nu \sim 15 \text{ cm}^{-1}$ , as shown in Fig. S3 in the Supplemental Material [26]. This results from a strain due to the change in lattice dimension caused by doping, as also observed in the synchrotron XRD. In addition to the frequency changes, the Raman scattering intensity of the  $E_g$  modes in comparison

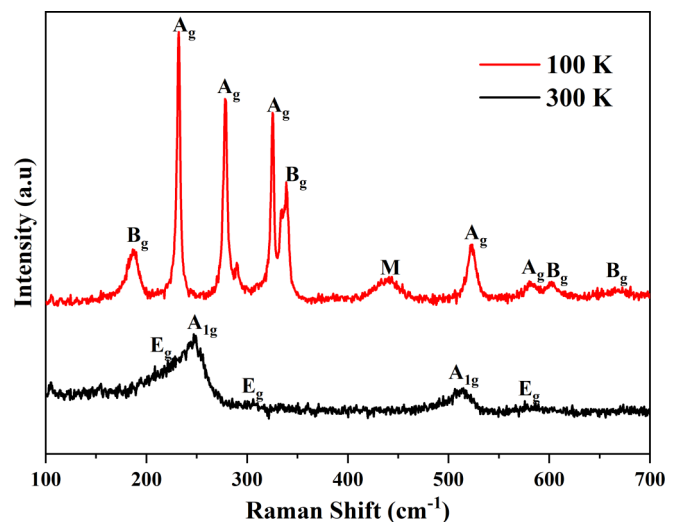


FIG. 4. Raman spectra of Ga-doped  $V_2O_3$  recorded at 300 and 100 K with different modes assigned corresponding to various vibrational symmetries.

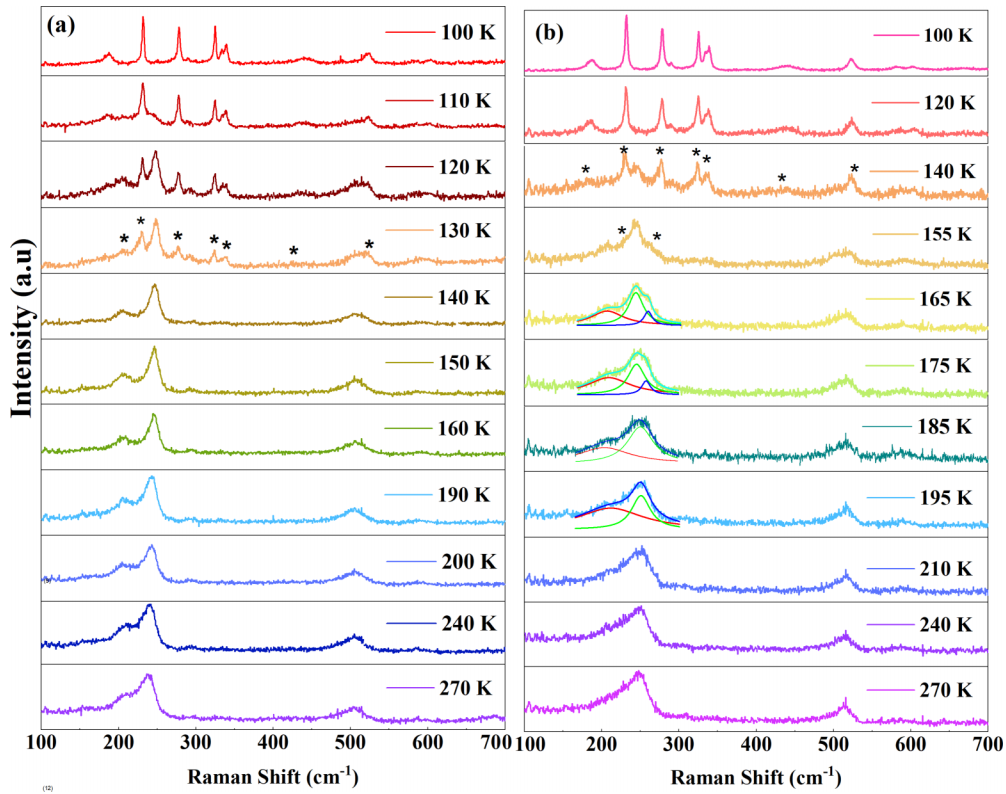


FIG. 5. Temperature-dependent Raman spectral stack plot of (a) undoped and (b) Ga-doped  $V_2O_3$ . Asterisks indicate the emergence of new peaks from the monoclinic phase.

with the  $A_{1g}$  modes decreased upon doping. Upon cooling the sample, distortion in the corundum unit cell leads to the occurrence of new Raman modes, indicating the appearance of a monoclinic phase. Two  $A_{1g}$  phonons of corundum structure lead to two  $A_g$  phonons of monoclinic structure. Each  $E_g$  phonon corresponds to a pair of  $A_g + B_g$  phonons, and a broad magnon peak is also seen, denoted as  $M$ . The broad peak seen at  $680\text{ cm}^{-1}$  corresponds to a  $B_g$  mode [32]. The evolutions of Raman spectra with temperature for  $V_2O_3$  and Ga-doped  $V_2O_3$  are shown in Figs. 5(a) and 5(b), respectively. The structural transition of  $V_2O_3$  is clear from the presence of the phonon modes belonging to the rhombohedral and the monoclinic phases at 270 and 100 K, respectively [see Fig. 5(a)]. As compared with the transition characteristics for a single crystal, the transition for a polycrystalline  $V_2O_3$  is not abrupt but gradual and extends over a broad temperature range. For polycrystalline  $V_2O_3$ , while cooling, we see that the Raman scattering modes of the monoclinic phase start appearing  $<130\text{ K}$ , but the rhombohedral phase coexists down to 110 K. The transition temperature is lowered most probably due to the stress and size effects present in the sample. Such phase coexistence features and lowering of  $T_c$  have been reported in thin films of  $V_2O_3$  [34–36].

The temperature dependence of the frequencies of Raman modes for Ga-doped  $V_2O_3$  is given in Figs. 6(a)–6(d). The change in phonon frequency with temperature can have contributions from different sources, such as change due to the variation of lattice parameters, anharmonicity, electron-phonon coupling, and spin-phonon coupling [37]. In general,

the temperature dependence of the phonon frequency  $\omega(T)$  follows the relation [37,38]:

$$\omega(T) = \omega_0 + \Delta\omega(T)_V + \Delta\omega(T)_{\text{anh}},$$

where  $\omega_0$  is the frequency at 0 K,  $\Delta\omega(T)_V$  is the volume contribution due to thermal expansion, and the third term  $\Delta\omega(T)_{\text{anh}} = C\{1 + [\frac{2}{\exp(\frac{h\omega_0}{2kT})} - 1]^{-1}\}$  describes the contribution from anharmonic interactions. In the Ga-doped sample, the temperature dependence of Raman shifts can be analyzed with the linear approximation at high temperatures down to 195 K, but the degeneracy of the two vibrations in the  $A_{1g}$  mode starts lifting, and the  $E_g$  mode at  $229\text{ cm}^{-1}$  displays a softening  $<195\text{ K}$  [see the slope changes in Figs. 6(a) and 6(b)]. It should be noted that Raman spectroscopy, being a local probe, can detect the subtle changes occurring like a tilting of the octahedra, change in bond angles or bond distances, etc., and serves as a prelude to the phase transition. Hence, a detailed study was done on the changes of the  $A_{1g}$  mode with temperature, and the result is shown in Fig. 6(a). Below 195 K, the  $A_{1g}$  mode started to display softening and broadening [see Figs. 5(b) and 6(a)]. From 180 K onwards, two peaks could be observed and fitted at 242 and  $255\text{ cm}^{-1}$ , respectively [Fig. 6(a)] and the intensity of the high-frequency mode decreases continuously with the decrease in temperature, whereas the intensity of the low-frequency mode gets enhanced. This change was also observed earlier in the Raman scattering study of Cr-doped  $V_2O_3$  [30]. Below 140 K, only one peak at  $245\text{ cm}^{-1}$  was observed, and the intensity of this mode started decreasing with temperature.

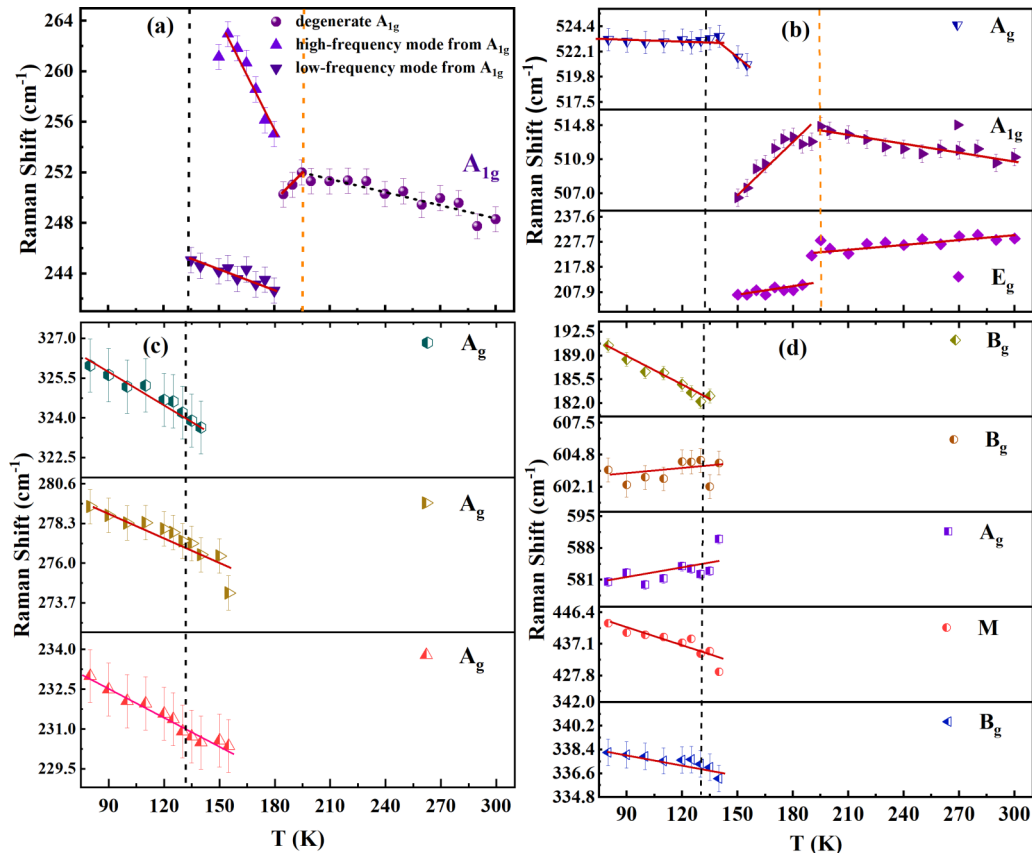


FIG. 6. Raman shift vs temperature plots of various Raman modes for Ga-doped  $V_2O_3$ . The dotted line represents the linear fit, and solid lines represent guides to the eye.

Eventually, the mode disappears at 127 K [Fig. 6(a)]. Some Raman modes corresponding to a monoclinic phase emerge from the background from 155 K [see Figs. 5(b) and 6(b)–6(d)], which suggests the coexistence of the monoclinic phase with the rhombohedral phase. However, the structural transition completes only at 127 K [Figs. 5(b) and 6(b)–6(d)]. We could not see the weak and broad magnon peak up to 135 K; this could probably be due to the background noise present. Below 135 K, the intensity of the magnon peak increases gradually during cooling [see Figs. 5(b) and 6(d)]. It is interesting to note that, in the case of polycrystalline undoped  $V_2O_3$ , the degeneracy lifting of the  $A_{1g}$  mode was not observed, and the new peaks emerged very clearly  $< 130$  K, coexisting with the rhombohedral phase [see Fig. 5(a)].

To study the magnetic transition and related properties, temperature-dependent zero-field-cooled (ZFC) and field-cooled (FC) magnetic susceptibility measurements of Ga-doped  $V_2O_3$  were carried out under an applied DC field of 100 Oe, shown in Fig. 7(a). The susceptibility drops at  $T_N \sim 185$  K, indicating the AFM ordering of the  $V^{3+}$  ion. This temperature is at least 25 K higher than that observed in undoped  $V_2O_3$ . An increase in  $T_N$  was also observed for 2.8% Cr-doped  $V_2O_3$  ( $T_N \sim 181$  K) [39]. Hence, it seems that the rise in  $T_N$  occurs irrespective of the magnetic nature of the doping impurity. Above  $T_N$ , the temperature dependence of susceptibility follows Curie-Weiss behavior with a negative  $\theta_{CW} \sim -655$  K. The calculated  $\mu_{\text{eff}}$  value per  $V^{3+}$  ion

for Ga-doped  $V_2O_3$  is  $2.93 \mu_B$ , which is comparable with the spin-only magnetic moment of the  $V^{3+}$  ion ( $2.84 \mu_B$ ). Below  $T_N$ , there is an irreversibility between the ZFC and FC curves with the susceptibility increasing below  $T \sim 100$  K [see Fig. 7(a)]. A similar result was reported, and its origin was attributed to uncompensated surface spins on the AFM nanoparticles [40,41]. Indeed, our scanning electron microscopy (SEM) measurements confirmed the presence of submicrometer-sized Ga-doped  $V_2O_3$  particles (Fig. S4 in the Supplemental Material [26]). To rule out the presence of any magnetic impurity in Ga-doped  $V_2O_3$ , we performed ICP-OES measurements which can detect elements with a concentration  $> 0.5$  ppm. Quantitatively, we found 94.6% vanadium and 5.4% gallium in the sample.

Further investigating the magnetic structure of Ga-doped  $V_2O_3$ , temperature-dependent NPD data were collected from 300 to 1.5 K at several temperatures. The corresponding NPD profiles are shown in Fig. 7(b). Upon cooling across 175 K, the symmetry changes from rhombohedral to monoclinic, and new magnetic peaks originate, indicating the occurrence of a structural and magnetic transition. Due to the monoclinic transition, Bragg peak  $(2 - 1 3)$  splits to give  $(3 1 0)$ ,  $(-1 2 1)$ , and  $(1 1 2)$  reflections. Additionally, magnetic peaks  $(0 1 0)$  and  $(0 0 1)$ , indicated with asterisks, evolve as the sample is cooled down to 1.5 K [see Fig. 7(b)]. The magnetic structure of Ga-doped  $V_2O_3$  is solved by analyzing NPD data collected  $< 175$  K using JANA2006 [22]. The magnetic peaks observed



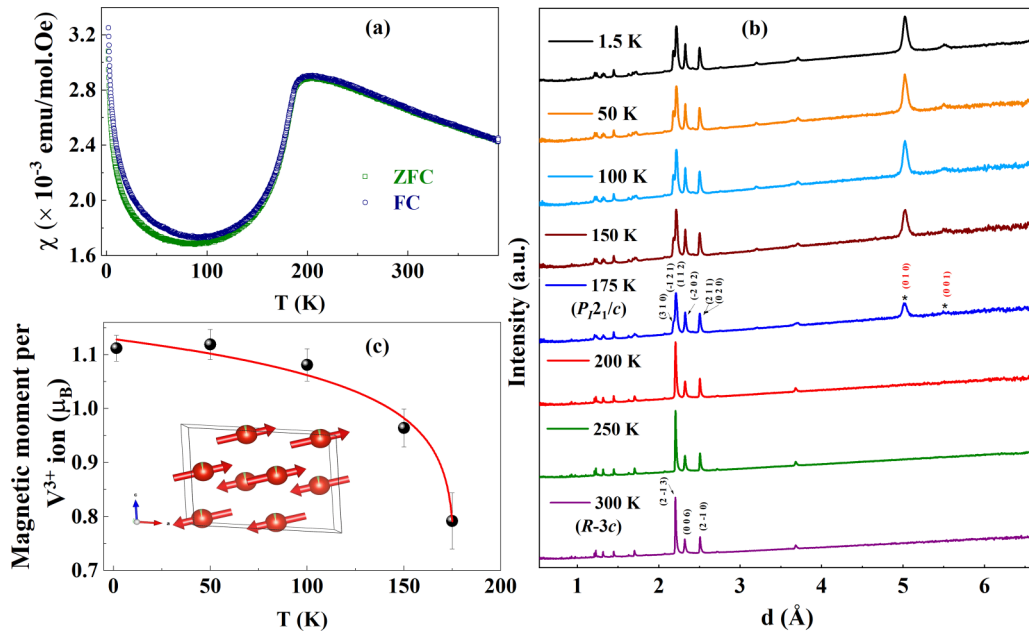


FIG. 7. (a) Temperature-dependent DC magnetic susceptibility curve. (b) Time-of-flight neutron powder diffraction (NPD) profiles collected using WISH detector bank with average  $2\theta$  of  $90^\circ$  at different temperatures, where the magnetic peaks are indicated by asterisk. (c) Temperature dependence of refined  $V^{3+}$  magnetic moment in the antiferromagnetic (AFM) lattice of Ga-doped  $V_2O_3$ . The magnetic structure of Ga-doped  $V_2O_3$  is shown as an inset in Fig. 7(c).

below  $T = 175$  K were indexed with the propagation vector  $k = (001)$ . Using the  $k$  vector, four possible magnetic (Shubnikov) space groups are obtained, which are  $P_12/c$ ,  $P_21/c$  with origin shift  $(\frac{1}{4}, \frac{1}{4}, \frac{1}{4})$ ,  $P_12_1/c$ , and  $P_12_1/c$  with origin shift  $(\frac{1}{4}, \frac{1}{4}, \frac{1}{4})$ . The magnetic space group  $P_12_1/c$  with origin shift  $(\frac{1}{4}, \frac{1}{4}, \frac{1}{4})$  exactly describes the diffraction profile obtained at low temperatures. This magnetic space group corresponds to the action of the  $mY_2^-$  irreducible representation. Rietveld refined time-of-flight NPD profiles of Ga-doped  $V_2O_3$  at 300 K (paramagnetic state) and 1.5 K (AFM state) are shown in Figs. S5(a) and S5(b), respectively, in the Supplemental Material [26]. The refined structural parameters obtained from the Rietveld refinement of 300 and 1.5 K data are displayed in Table S1 in the Supplemental Material [26]. The refined magnetic moment values for different temperatures are shown in Fig. 7(c). The temperature-dependent magnetic moment of the  $V^{3+}$  ion follows the mean-field power law behavior [42]  $m(T) = m_o (1 - \frac{T}{T_N})^\beta$ . The magnetic structure of Ga-doped  $V_2O_3$  consists of vanadium moments aligned ferromagnetically within the  $(0, 1, 0)$  monoclinic plane but antiparallel with the neighboring plane, as shown in the inset of Fig. 7(c). The obtained magnetic structure is similar to that reported for undoped  $V_2O_3$  [43].

To study the thermal transport properties, temperature-dependent heat capacity divided by temperature ( $C_p/T$ ) was measured on Ga-doped  $V_2O_3$  and is shown in Fig. 8(a). The  $\lambda$ -shaped anomaly at 185 K corresponds to magnetic and structural transition. Entropy change across the phase transition of Ga-doped  $V_2O_3$  is shown in the inset (top left) of Fig. 8(a). The calculated entropy change across the magnetic and structural transition is  $\Delta S \sim 3.65 \text{ J mol}^{-1} \text{ K}^{-1}$ , which is less than undoped  $V_2O_3$  ( $\Delta S \sim 10.8 \text{ J mol}^{-1} \text{ K}^{-1}$ ) [44,45].

We analyzed the low-temperature region ( $T < 15$  K) using the approximate Debye model  $C(T) = \beta T^3$ , where the  $\beta T^3$  term accounts for phononic contribution with coefficient  $\beta = \frac{12\pi^4 NR}{5\theta_D^3}$ . Here,  $N$  and  $R$  are the number of atoms per formula unit and gas constant, respectively. This resulted in a poor fit to the heat capacity data. Considering the low-temperature DC magnetization and SEM measurements, it is possible that the uncompensated surface spins also contribute to the low-temperature heat capacity. Hence, a ferromagnetic term [46]  $\alpha T^{3/2}$  was considered which gave the best fit. The heat capacity data fitted with the equation  $C(T) = \beta T^3 + \alpha T^{3/2}$  is shown in the inset (bottom right) of Fig. 8(a). The fit returned  $\beta = 1.675(1) \times 10^{-4} \text{ J mol}^{-1} \text{ K}^{-4}$  and the Debye temperature ( $\theta_D$ ) of 387.52(4) K. The coefficient for the magnetic term  $\alpha = 12.7(1) \text{ mJ mol}^{-1} \text{ K}^{-5/2}$  is comparable with that of dilute magnetic alloys [47]. The DSC curve obtained from both heating and cooling measurements further confirms that Ga-doped  $V_2O_3$  undergoes a structural transition at  $T \sim 189$  K, as shown in Fig. 8(b).

To investigate the electrical transport properties, temperature-dependent resistivity measurements were carried out for Ga-doped  $V_2O_3$  and undoped  $V_2O_3$  while heating and cooling in the temperature range 120–300 K and are shown in Fig. 9(a). At 300 K, the resistivity value in the doped sample is  $10^3$  times higher than that of the undoped  $V_2O_3$ . The positive temperature coefficient of  $\rho(T)$  in  $V_2O_3$  is consistent with the metallic nature of the sample. On the other hand, the doped sample shows a negative slope, indicating the weakly insulating behavior [see Fig. 9(a)]. Undoped  $V_2O_3$  shows a MIT with a thermal hysteresis of 13 K between the cooling (163 K) and warming (175 K) curves, confirming the first-order nature of the transition [see Fig. 9(a)]. In contrast,

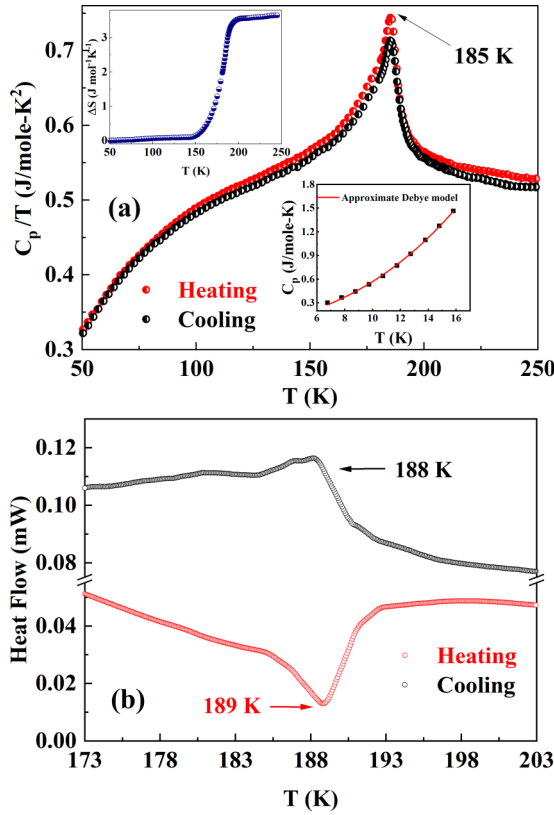


FIG. 8. (a) Temperature-dependent heating and cooling  $C_p/T$  curve of Ga-doped  $V_2O_3$  measured from 50–250 K. Approximate Debye fit to the  $C_p$  vs  $T$  ( $T < 15$  K) curve is shown in the inset (bottom right), and entropy change across magnetic and structural transition plotted with respect to temperature is shown in the inset (top left). (b) Differential scanning calorimetric curves were obtained for Ga-doped  $V_2O_3$  during heating and cooling cycles.

the  $\rho(T)$  of the doped sample exhibits only a change of slope at  $T \sim 185$  K without any thermal hysteresis. Below 185 K, resistivity begins to increase monotonously and reaches  $10^5 \Omega \text{ cm}$  at 120 K. Such a state of the system with huge resistivity could be considered as insulating. It is reported that undoped  $V_2O_3$  shows the anomalous behavior of resistivity in the high-temperature region 300–600 K which is attributed to changes in V-V distance due to the magnetoelastic effect [48]. However, we do not see any anomaly in the doped sample in the temperature range 200–390 K, as shown in Fig. 9(b). The resistivity behavior of Ga-doped  $V_2O_3$  is similar to the results observed for  $V_2O_3$  thin films grown on annealed sapphire [49]. The semiconducting behavior of these films is attributed to the increased impurity scattering due to the structural disorder and the defects present in the films. Additionally, oxygen inhomogeneities play a significant role in the MIT temperature and suppression of thermal hysteresis [50]. Epitaxially grown  $V_2O_3$  thin films in low oxygen pressures showed semiconducting behavior because of the greater Anderson localization arising from defects, triggering the earlier onset of the insulating state. Such a PMI-AFI transition was observed for undoped and 3% Cr-doped  $V_2O_3$  thin film induced through enhancing the trigonal distortion by optimizing synthesis conditions [36]. Also, the structural

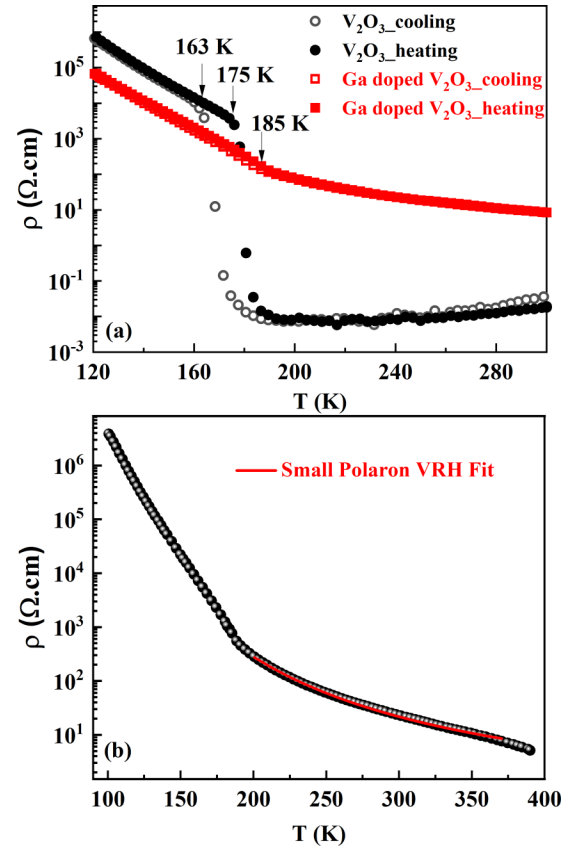


FIG. 9. (a) Temperature-dependent heating and cooling resistivity curve of undoped and Ga-doped  $V_2O_3$ . (b) Temperature-dependent resistivity curve of Ga-doped  $V_2O_3$  measured from 100–390 K with the fit obtained using variable range hopping (VRH) model for small polarons.

inhomogeneities resulting from synthesis conditions can contribute to higher resistivity values in the PMI phase due to enhanced carrier scattering [36].

To understand the nature of electrical conductivity in the doped sample, we fitted the resistivity curve in the weakly insulating region 195–370 K, as shown in Fig. 9(b), with the variable range hopping (VRH) model for small polarons which is expressed by the equation [51]:

$$\rho = BT \exp\left[\frac{E_1}{k_B T} + \left(\frac{T_o}{T}\right)^{1/4}\right],$$

where  $B = \frac{k_B}{q^2 \vartheta_0 \gamma_0}$ ,  $k_B$  is the Boltzmann constant,  $\gamma_0$  is the constant related to the hopping rate, and  $\vartheta_0$  is the characteristic frequency of the phonons. Here,  $E_1$  is the energy difference between initial and intermediate states. Here,  $T_o$  is the characteristic temperature described by the equation:

$$T_o = \frac{18\alpha^3}{N(E)k_B},$$

where  $\frac{1}{\alpha}$  is the localization length, and  $N(E)$  is the density of states. The obtained values of  $E_1$  and  $T_o$  are 144(5) meV and  $1.9 \times 10^3$  K, respectively. Here, the presence of cation disorder in the system acts as a potential barrier for the

charge carriers and hence favors VRH over nearest-neighbor hopping.

This study of the effects of Ga doping on properties of  $V_2O_3$  helps to uncover the interdependency of occurrence of various phase transitions, i.e., structural, magnetic, and MIT. As discussed before, the subtle changes in the Raman modes, i.e., the lifting of the degeneracy of  $A_{1g}$  modes, indicates the onset of a structural phase transition much above  $T_N$ , even though there is no sign of Raman modes corresponding to the monoclinic phase. Hence, the structural distortion in the corundum unit cell precedes the magnetic and insulator-insulator transition. This suggests that magnetic transition requires subtle changes in the tilting of octahedra and not the complete phase transition to the monoclinic phase. Recent density functional theory studies conducted using the generalized gradient approximation revealed that the occurrence of the monoclinic structural change is independent of magnetism, but they reinforce each other in the  $V_2O_3$  case [52].

On the other hand, the magnetic and electronic transitions appear to occur at the same temperature ( $T_N$  or  $T_{II} \sim 185$  K), indicating the possibility of the interdependency of magnetism and electronic phase transitions. Hubbard model calculations reported by Trastoy *et al.* [7] confirm the coupling of AFM ordering with electronic transport in  $V_2O_3$  thin films, across MIT. The gradual change in resistivity across PMI-AFI phase transition observed in Ga-doped  $V_2O_3$  is like that of 3 at. % Cr-doped  $V_2O_3$ . As the doping concentration of Cr in  $V_2O_3$  reaches a critical value, two different metal-to-insulator phase transitions coincide and subsequently bypass the metallic state to give a PMI-to-AFI transition [30,53]. Similarly, it seems that 4% Ga doping is the critical doping limit, which leads to PMI-to-AFI phase transition at 185 K. In strained  $V_2O_3$  thin films, it is shown that the  $A_{1g}$  phonon mode in the PMM phase strongly varies with the trigonal distortion by tuning the parameter  $c/a$  and directly determines the PMM-AFI characteristics [36]. The PMM phase persists in the  $c/a$  range of 2.803 to 2.862, and by decreasing the  $c/a$  ratio to 2.786–2.781, the PMI phase appears. This is consistent with the 4% Ga-doped  $V_2O_3$ , where the  $c/a$  ratio is 2.7793(9), causing significant trigonal distortion, leading to the PMI phase at ambient conditions. Also, the V-V distance between the face-shared octahedra plays an important role in determining the electronic structure of  $V_2O_3$ . As discussed earlier, at ambient conditions, there is an increase of V-V distance in the Ga-doped sample which could significantly reduce the hybridization strength between the  $3d$  orbitals, thus constraining the hopping of electrons. Extended x-ray absorption fine structure studies for Cr-doped  $V_2O_3$  showed that, during monoclinic distortion, the V-V bond of every vanadium pair situated along the  $z$  axis tilts toward the negative side of the  $y$  axis (monoclinic  $b_m$  axis), breaking the trigonal symmetry, and causes further elonga-

tion of V-V distance [54]. A possible mechanism for the PMI-to-AFI transition has been proposed in which the nearest neighbor V pair with degenerate  $3d$  orbitals were considered using a many-body approach. In this model, the elongation of the V-V bond along the  $c$  axis is considered, and the resultant reduction in the hybridization strength due to spin-lattice coupling is determined by comparing the  $a_1$  orbital occupancy across the MIT [55]. We speculate that the PMI-to-AFI phase transition is mainly driven by trigonal distortion and elongation of V-V bond during structural distortion in Ga-doped  $V_2O_3$ . Conclusively, structural, magnetic, and electronic phase transitions occurring in  $V_2O_3$  do not seem to have a joint driving force; instead, these are cooperative with each other.

#### IV. CONCLUSIONS

Decoupling of structural phase transition from magnetic and electronic transition is evidenced by gallium doping in  $V_2O_3$ . Unlike  $V_2O_3$ , 4% gallium-doped  $V_2O_3$  shows splitting of the  $A_{1g}$  mode due to degeneracy lifting near the onset of the structural phase transition at 195 K. Temperature-dependent synchrotron XRD studies revealed phase coexistence of rhombohedral-to-monoclinic phase in the temperature region 180–127 K, which is consistent with Raman spectroscopic studies. Magnetization and heat capacity measurements showed paramagnetic-to-AFM transition at 185 K in Ga-doped  $V_2O_3$ , which is 25 K higher than undoped  $V_2O_3$ . Additionally, the PMI-to-AFI transition occurs with no hysteresis at 185 K.

#### ACKNOWLEDGMENTS

The authors would like to thank the Sheikh Saqr Laboratory and International Centre for Materials Science at Jawaharlal Nehru Centre for Advanced Scientific Research (JNCASR) for providing experimental facilities. A.S. and C.N. acknowledge Department of Science and Technology (DST) and Science and Engineering Research Board (SERB), India, and the government of India for financial support. C.N. and A.J. would like to acknowledge JNCASR Technical Research Centre for the Raman facility. P.N.S. and A.J. acknowledge JNCASR for providing a research fellowship (No. JNC/S0484 and No. JNC/S0752). P.N.S. acknowledges Mr. Suhas K. T. for ICP-OES measurements and related analysis. R.M. acknowledges the Dean, Faculty of Science, National University of Singapore for supporting this work while on sabbatical leave to JNCASR. R.M. also acknowledges the Ministry of Education, Singapore (Grant No. R144-000-422-114). The authors acknowledge the Science and Technology Facility Council for the provision of neutron beam time on the WISH instrument.

[1] D. McWhan, A. Menth, J. Remeika, W. F. Brinkman, and T. Rice, Metal-insulator transitions in pure and doped  $V_2O_3$ , *Phys. Rev. B* **7**, 1920 (1973).

[2] P. Dernier and M. Marezio, Crystal structure of the low-temperature antiferromagnetic phase of  $V_2O_3$ , *Phys. Rev. B* **2**, 3771 (1970).

- [3] N. Mott, The transition to the metallic state, *Philos. Mag.* **6**, 287 (1961).
- [4] N. Mott, On the transition to metallic conduction in semiconductors, *Can. J. Phys.* **34**, 1356 (1956).
- [5] N. F. Mott, The basis of the electron theory of metals with special reference to the transition metals, *Proc. Phys. Soc. A* **62**, 416 (1949).
- [6] J. Slater, Magnetic effects and the Hartree-Fock equation, *Phys. Rev.* **82**, 538 (1951).
- [7] J. Trastoy, A. Camjayi, J. del Valle, Y. Kalcheim, J. P. Crocombette, D. A. Gilbert, J. A. Borchers, J. E. Villegas, D. Ravelosona, M. J. Rozenberg *et al.*, Magnetic field frustration of the metal-insulator transition in  $V_2O_3$ , *Phys. Rev. B* **101**, 245109 (2020).
- [8] I. Lo Vecchio, L. Baldassarre, F. D'Apuzzo, O. Limaj, D. Nicoletti, A. Perucchi, L. Fan, P. Metcalf, M. Marsi, and S. Lupi, Optical properties of  $V_2O_3$  in its whole phase diagram, *Phys. Rev. B* **91**, 155133 (2015).
- [9] G. Keller, K. Held, V. Eyert, D. Vollhardt, and V. Anisimov, Electronic structure of paramagnetic  $V_2O_3$ : strongly correlated metallic and Mott insulating phase, *Phys. Rev. B* **70**, 205116 (2004).
- [10] D. B. McWhan, T. M. Rice, and J. P. Remeika, Mott Transition in Cr-Doped  $V_2O_3$ , *Phys. Rev. Lett.* **23**, 1384 (1969).
- [11] W. R. Robinson, High-temperature crystal chemistry of  $V_2O_3$  and 1% chromium-doped  $V_2O_3$ , *Acta Cryst. B* **31**, 1153 (1975).
- [12] D. McWhan and J. Remeika, Metal-insulator transition in  $(V_{1-x}Cr_x)_2O_3$ , *Phys. Rev. B* **2**, 3734 (1970).
- [13] D. S. Toledano, P. Metcalf, and V. E. Henrich, Surface conditions for the observation of metal-insulator transitions on Cr-doped  $V_2O_3$ , *Surf. Sci.* **449**, 19 (2000).
- [14] H. V. Keer, D. L. Dickerson, H. Kuwamoto, H. L. C. Barros, and J. M. Honig, Heat capacity of pure and doped  $V_2O_3$  single crystals, *J. Solid State Chem.* **19**, 95 (1976).
- [15] C. Tenailleau, E. Suard, J. Rodriguez-Carvajal, and P. Lacorre, Influence of Mo-doping on the magnetic properties of  $V_2O_3$ , *J. Magn. Magn. Mater.* **278**, 57 (2004).
- [16] P. Rozier, A. Ratuszna, and J. Galy, Comparative structural and electrical studies of  $V_2O_3$  and  $V_{2-x}Ni_xO_3$  ( $0 < x < 0.75$ ) solid solution, *Z. anorg. allg. Chem.* **628**, 1236 (2002).
- [17] Y. Ding, C.-C. Chen, Q. Zeng, H.-S. Kim, M. J. Han, M. Balasubramanian, R. Gordon, F. Li, L. Bai, D. Popov *et al.*, Novel High-Pressure Monoclinic Metallic Phase of  $V_2O_3$ , *Phys. Rev. Lett.* **112**, 056401 (2014).
- [18] F. Fauth, I. Peral, C. Popescu, and M. Knapp, The new material science powder diffraction beamline at ALBA synchrotron, *Powder Diffr.* **28**, S360 (2013).
- [19] F. Fauth, R. Boer, F. Gil-Ortiz, C. Popescu, O. Vallcorba, I. Peral, D. Fullà, J. Benach, and J. Juanhuix, The crystallography stations at the ALBA synchrotron, *Eur. Phys. J. Plus* **130**, 160 (2015).
- [20] H. Rietveld, A profile refinement method for nuclear and magnetic structures, *J. Appl. Crystallogr.* **2**, 65 (1969).
- [21] T. Roisnel and J. Rodríguez-Carvajal, WINPLOTR: A Windows tool for powder diffraction pattern analysis, *Mater. Sci. Forum* **378**, 118 (2001).
- [22] V. Petříček, M. Dušek, and L. Palatinus, Crystallographic computing system JANA2006: General features, *Z. Kristallogr. Cryst. Mater.* **229**, 345 (2014).
- [23] R. Saha, F. Fauth, V. Caignaert, and A. Sundaresan, Coexistence of G- and C-type orbital ordered phases and its correlation with magnetization reversal in  $YVO_3$ , *Phys. Rev. B* **95**, 184107 (2017).
- [24] X. Li, Y. Wang, W. Liu, G. Jiang, and C. Zhu, Study of oxygen vacancies' influence on the lattice parameter in ZnO thin film, *Mater. Lett.* **85**, 25 (2012).
- [25] D. S. Aidhy, B. Liu, Y. Zhang, and W. J. Weber, Chemical expansion affected oxygen vacancy stability in different oxide structures from first principles calculations, *Comput. Mater. Sci.* **99**, 298 (2015).
- [26] See Supplemental Material at <http://link.aps.org/supplemental/10.1103/PhysRevB.105.064103> for details of synchrotron XRD, temperature evolution of structural phase transition, Raman spectra, SEM images, Rietveld refined time of flight NPD profiles, and tabulated structural parameters.
- [27] S. Chen, J. E. Hahn, C. E. Rice, and W. R. Robinson, The effects of titanium or chromium doping on the crystal structure of  $V_2O_3$ , *J. Solid State Chem.* **44**, 192 (1982).
- [28] P. D. Dernier, The crystal structure of  $V_2O_3$  and  $(V_{0.962}Cr_{0.0382})_2O_3$  near the metal-insulator transition, *J. Phys. Chem. Solids* **31**, 2569 (1970).
- [29] N. Kuroda and H. Fan, Raman scattering and phase transitions of  $V_2O_3$ , *Phys. Rev. B* **16**, 5003 (1977).
- [30] C. Tatsuyama and H. Y. Fan, Raman scattering and phase transitions in  $V_2O_3$  and  $(V_{1-x}Cr_x)_2O_3$ , *Phys. Rev. B* **21**, 2977 (1980).
- [31] E. Cowley, Symmetry properties of the normal modes of vibration of calcite and  $\alpha$ -corundum, *Can. J. Phys.* **47**, 1381 (1969).
- [32] P. Shvets, O. Dikaya, K. Maksimova, and A. Goikhman, A review of Raman spectroscopy of vanadium oxides, *J. Raman Spectrosc.* **50**, 1226 (2019).
- [33] U. Fano, Effects of configuration interaction on intensities and phase shifts, *Phys. Rev.* **124**, 1866 (1961).
- [34] X. B. Chen, J. H. Shin, H. T. Kim, and Y. S. Lim, Raman analyses of co-phasing and hysteresis behaviors in  $V_2O_3$  thin film, *J. Raman Spectrosc.* **43**, 2025 (2012).
- [35] A. Rúa, K. Echeverría, B. Ayala, G. A. Goenaga, S. Lysenko, and F. E. Fernández, Toward reproducible metal-insulator transition characteristics in  $V_2O_3$  thin films sputter-deposited on glass, *J. Appl. Phys.* **124**, 205301 (2018).
- [36] L. Hu, C. Xie, S. J. Zhu, M. Zhu, R. H. Wei, X. W. Tang, W. J. Lu, W. H. Song, J. M. Dai, R. R. Zhang *et al.*, Unveiling the mechanisms of metal-insulator transitions in  $V_2O_3$ : the role of trigonal distortion, *Phys. Rev. B* **103**, 085119 (2021).
- [37] E. Granado, A. Garcia, J. Sanjurjo, C. Rettori, I. Torriani, F. Prado, R. Sánchez, A. Caneiro, and S. Oseroff, Magnetic ordering effects in the Raman spectra of  $La_{1-x}Mn_xO_3$ , *Phys. Rev. B* **60**, 11879 (1999).
- [38] M. Balkanski, R. Wallis, and E. Haro, Anharmonic effects in light scattering due to optical phonons in silicon, *Phys. Rev. B* **28**, 1928 (1983).
- [39] A. Bombardi, F. de Bergevin, S. Di Matteo, L. Paolasini, P. A. Metcalf, and J. M. Honig, Precursor symmetry breaking in Cr doped  $V_2O_3$ , *Physica B* **345**, 40 (2004).
- [40] R. Bhowmik and R. Ranganathan, Enhancement of surface magnetization in antiferromagnetic nanoparticles, *Solid State Commun.* **141**, 365 (2007).

- [41] I. Mjejri, A. Rougier, and M. Gaudon, Low-cost and facile synthesis of the vanadium oxides  $V_2O_3$ ,  $VO_2$ , and  $V_2O_5$  and their magnetic, thermochromic and electrochromic properties, *Inorg. Chem.* **56**, 1734 (2017).
- [42] P. W. Egolf and K. Hutter, The mean field theories of magnetism and turbulence, *Entropy* **19**, 589 (2017).
- [43] H. Kuwamoto, W. R. Robinson, and J. M. Honig, Magnetic structure of the low temperature antiferromagnetic phase of  $V_2O_3$ , *J. Solid State Chem.* **24**, 389 (1978).
- [44] D. McWhan, J. Remeika, T. Rice, W. F. Brinkman, J. Maita, and A. Menth, Electronic Specific Heat of Metallic Ti-doped  $V_2O_3$ , *Phys. Rev. Lett.* **27**, 941 (1971).
- [45] O. Lyakh, V. I. Surikov, V. Surikov, and N. Prokudina, Magnetic susceptibility and heat capacity of  $V_2O_3$  and  $V_{1.973}Me_{0.020}O_3$  ( $Me = Fe, Cr, \text{ and } Al$ ), *Russ. Phys. J.* **55**, 116 (2012).
- [46] J. Morrison and D. Newsham, Analyses of low-temperature heat capacities containing two or more contributions: Application to the rare earth metals, *J. Phys. C Solid State Phys.* **1**, 370 (1968).
- [47] J. Thomson and J. Thompson, Low-temperature excitations in spin glasses: Evidence for a  $T^{3/2}$  behaviour, *J. Phys. F Met. Phys.* **11**, 247 (1981).
- [48] B. Belbeoch, R. Kleinberger, and M. Roulliy, Correlation between the high temperature anomalies in  $V_2O_3$  and the lattice parameters, *J. Phys. Chem. Solids* **39**, 1007 (1978).
- [49] J. Brockman, M. Samant, K. Roche, and S. Parkin, Substrate-induced disorder in  $V_2O_3$  thin films grown on annealed *c*-plane sapphire substrates, *Appl. Phys. Lett.* **101**, 051606 (2012).
- [50] J. Brockman, N. Aetukuri, T. Topuria, M. Samant, K. Roche, and S. Parkin, Increased metal-insulator transition temperatures in epitaxial thin films of  $V_2O_3$  prepared in reduced oxygen environments, *Appl. Phys. Lett.* **98**, 152105 (2011).
- [51] Y. Sun, X. Xu, and Y. Zhang, Variable-range hopping of small polarons in mixed-valence manganites, *J. Phys. Condens. Matter* **12**, 10475 (2000).
- [52] D. Grieger and M. Fabrizio, Low-temperature magnetic ordering and structural distortions in vanadium sesquioxide  $V_2O_3$ , *Phys. Rev. B* **92**, 075121 (2015).
- [53] M. Yethiraj, S. Werner, W. Yelon, and J. Honig, Phonon anomalies and the magnetic transition in pure and Cr-doped  $V_2O_3$ , *Phys. Rev. B* **36**, 8675 (1987).
- [54] C. Meneghini, S. Di Matteo, C. Monesi, T. Neisius, L. Paolasini, S. Mobilio, C. Natoli, P. A. Metcalf, and J. M. Honig, Antiferromagnetic-paramagnetic insulating transition in Cr-doped  $V_2O_3$  investigated by EXAFS analysis, *J. Phys. Condens. Matter* **21**, 355401 (2009).
- [55] A. Tanaka, Electronic Structure and Phase Transition in  $V_2O_3$ : importance of  $3d$  spin-orbit interaction and lattice distortion, *J. Phys. Soc. Jpn.* **71**, 1091 (2002).